Self-Assembly of Wireframe DNA Nanostructures from Junction Motifs

Kai Huang, Donglei Yang, Zhenyu Tan, Silian Chen, Ye Xiang, Yongli Mi, Chengde Mao,* and Bryan Wei*

Abstract: Wireframe frameworks have been investigated for the construction of complex nanostructures from a scaffolded DNA origami approach; however, a similar framework is yet to be fully explored in a scaffold-free "LEGO" approach. Herein, we describe a general design scheme to construct wireframe DNA nanostructures entirely from short synthetic strands. A typical edge of the resulting structures in this study is composed of two parallel duplexes with crossovers on both ends, and three, four, or five edges radiate out from a certain vertex. By using such a self-assembly scheme, we produced planar lattices and polyhedral objects.

As a latecomer in DNA nanotechnology, the scaffolded DNA origami method has showcased its self-assembly power, and all kinds of complex structures have been constructed based on the method.[1] On the other hand, DNA self-assembly from short strands without the guidance from a scaffold, which was introduced to the field much earlier,[2] has also emerged recently as a method for constructing complex addressable structures.[3] After a well-received introduction of complex addressable structures from single-stranded tiles/bricks, several classic motifs in DNA nano-technology have been adopted to construct addressable nanostructures.[4] The successful results have shown that the classic motifs are capable of self-assembly into not only micrometer periodic lattices with few repetitive motif species but also complex addressable structures with hundreds or even thousands of distinct motif species.

The structural motifs of this report are modified from those from earlier studies.[4b,5] Instead of regular lattice type

(i.e., compact helices in parallel) of arrangement, armed motifs are designed to form lattice-free wireframe structures. To begin with, we use armed motifs to construct 2D wireframe structures of full addressability. Then, we also demonstrate that single-stranded DNA (ssDNA) or double-stranded DNA (dsDNA) linkers at a specific vertex can result in a desired angle between the corresponding arms. Moreover, the similar designs are also applied to form extended structures from repetitive motifs. Besides planar wireframe structures, poly-hedral objects, such as octahedrons and icosahedrons, are also constructed. The design principle presented in this study is a generally applicable to different types of addressable wireframe architectures.

Different from the earlier designs, in which a typical double-duplex edge is bundled by crossovers in the middle of the helices,[1g,h,2d,h] a typical edge of all the structures presented in this study has two duplexes bundled by cross-overs on both ends (i.e., crossovers at vertices).

We first designed Y-shaped motifs to form an addressable honeycomb grid. The resulting honeycomb grid can be viewed as individual Y-shaped motifs intertwined with one another by their matching arms. A Y-shaped motif is divided into three 52-nt strands, shown in different colors in colors Figure 1A. Each component strand consists of four 13-nt domains (Supporting Information, Figure S1). Each arm of a Y-motif is paired with an arm from a matching Y-motif for an edge of two bundled helices (each with 2.5 helical turns) with crossovers on both ends. The symmetric design ensures that there is only one nicking point for every component duplex. The full honeycomb grid consists of 77 distinct Y-motifs and

---

[*] K. Huang, Z. Tan, Prof. Dr. B. Wei
School of Life Sciences, Tsinghua University-Peking University Center for Life Sciences, Center for Synthetic and Systems Biology
Tsinghua University
Beijing 100084 (China)
E-mail: bw@tsinghua.edu.cn

Dr. D. Yang, Prof. Dr. Y. Mi
School of Chemical Science and Engineering, Tongji University
Shanghai 200092 (China)

Dr. D. Yang
Institute of Molecular Medicine (IMM), Renji Hospital, Shanghai Jiao Tong University, School of Medicine
Shanghai 200127 (China)

S. Chen, Prof. Dr. Y. Xiang
Center for Infectious Disease Research, Collaborative Innovation Center for Diagnosis and Treatment of Infectious Diseases, Beijing Advanced Innvation Center for Structural Biology, Department of Basic Medical Sciences, School of Medicine, Tsinghua University
Beijing 100084 (China)

S. Chen
School of Life Sciences, Peking University
Beijing 100084 (China)

Prof. Dr. Y. Mi
Department of Chemical and Biological Engineering, Hong Kong University of Science and Technology
Kowloon, Hong Kong SAR (China)

Prof. Dr. C. Mao
Department of Chemistry, Purdue University
West Lafayette, IN 47907 (USA)
E-mail: mao@purdue.edu

Z. Tan
Present address: Biophysics Program, University of Michigan
Ann Arbor, MI 48109 (USA)

Supporting information and the ORCID identification number(s) for the author(s) of this article can be found under:
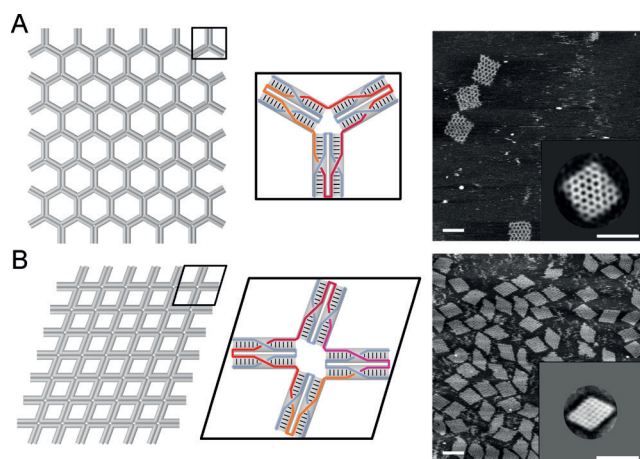https://doi.org/10.1002/anie.201906408.

Figure 1. 2D addressable wireframe structures from armed motifs.
A) Addressable honeycomb grid with Y-shaped (3-arm) motifs.
B) Addressable rhombic grid with X-shaped (4-arm) motifs. Panels
from left to right: Schematics of full structures, schematics of
representative motifs, and AFM images (scale bars = 100 nm). Insets:
Reference-free class average calculated from single-particle AFM micro-
graphs [N = 11 in (A) and N = 84 in (B)].

there are 14 rows with five or six Y-motifs for each row (256
distinct strands for the full structure). Similarly, we designed
X-shaped motifs to form an addressable rhombic grid.
Following the similar design principles, four nicking points
correspond to four strands for each X-shaped contour (each
component strand is 52-nt long with four 13-nt domains)
(Figure 1B and Figure S2). Individual X-motifs matching one
another to form a rhombic grid composed of 42 X-motifs
(seven rows by six columns; 194 distinct strands for the full
structure).

After agarose gel electrophoresis, a dominant band was
presented for each addressable structure (including ones
introduced later in this report), indicating a successful
formation of the structure. Atomic force microscopy (AFM)
images revealed the desired morphologies of honeycomb or
rhombic grid with the expected dimensions and patterns
(Figure 1, right panels). Detailed measurements can be found
in Table S1. The formation of single Y- and X-motifs was
characterized by agarose gel electrophoresis (Figure S3).
Notably, the X-shaped motifs resulted in rhombic, instead
of tetragonal, grids; and correspondingly, the central cavity of
the motif took a rhombus shape instead of square shape. An
adjacent pair of angles of an X-shaped vertex were circa 110°
and circa 70°, instead of both 90°. This is presumably because
of the compromise between two conflicting factors; max-
imizing base stacking between adjacent aromatic nucleobases
at the vertices and minimizing electrostatic repulsion among
the DNA backbones. Similar angle preferences have also
been observed previously in other systems that involve 4-way
branched motifs, though the exact angle values were differ-
ent.[6]

For a 3-fold symmetric arrangement of the Y-motif, the
angles between any two arms are supposed to be 120° because
the central cavity has an undeformable triangular shape.
Indeed, circa 120° angles were observed in the corresponding
AFM image (Figure 1 A). The observed value of circa 120° in

the Y-motif design was close to the observed value of circa
110° in the X-motif design, suggesting that similar local vertex
structures between adjacent arms existed in both motifs. The
geometry of the Y-motif was subjected to adjustment. For
example, when a 10-bp duplex segment was placed at one of
the three crossover points between adjacent arms of a certain
vertex, the geometry of the central cavity would change,
leading an angle change from circa 120° to circa 150°.
Consequently, Y-shaped vertices deformed toward a T-
shape (Figure 2 A and Figure S4). Similar angle control was
applied to X-shaped vertices of the rhombic lattice (Fig-
ure 2 B and Figure S5). The incorporation of additional
duplex segments (10 bp) led to an angle change from circa
110°/70° of the X-shaped vertices to circa 90° of the cross-
shaped vertices. (Figure 2 B). As shown in averaged AFM
images of structures with angle control (Figure 2 A and B,
insets of right panels), the implementation strategy was
effective (Table S1). However, such a control was not precise,
and angles varied from junction point to junction point and
from structure to structure. When the linker of each Y-shaped
vertex was kept unpaired as ssDNA instead of dsDNA, the
circa 150° angles of the grid became less specified because of
the unbalanced base stacking (Figure 2 C and Figure S6). Self-
assembly of the grids from X-motifs with one or two 10-nt
single-stranded linker(s) (three or two crossover points
without linkers) at each vertex was also investigated. For an
X-shaped vertex with two 10-nt single-stranded linkers at
crossover points of opposing positions, two pairs of adjacent
arms without any linkers at the crossover points tended to
have a strong base stacking interaction and the vertex became
H-shaped. Hence, a diagonal stripe pattern was presented for
the grid (Figure 2 D and Figure S6). For an X-shaped vertex
with one 10-nt single-stranded linker, the single linker at
a certain vertex resulted in uncertainty in the stacking
orientation. Each of the two stacking orientations results in
a specific local pattern. Consequently, a chimera of the
rhombic pattern and diagonal stripe pattern was presented for
the grid (Figure 2 E and Figure S6). The results with unpaired
linkers clearly show that base stacking at the crossover point
between adjacent arms can determine the general geometry of
a vertex. The insertion of single-stranded linkers across
arms weakens or cancels the stacking force and brings in
flexibility to the corresponding vertex.

The same motifs were also implemented in a repetitive
fashion for construction of extended structures. For example,
a number of X-motifs (4 × 4 array with 16 motifs) or Y-motifs
(2 × 3 array with 6 motifs) served as a repetitive unit cell for
the construction of a 1D extended ribbon. Samples after
annealing were subjected to AFM imaging. 1D ribbons with
desired widths and texture details under AFM shows the
successful self-assembly (Figure 3 A,B; Figures S8 and S9). In
particular, we designed one continuous strand consisting of
six 16-nt domains (96-nt full length) as a full Y-motif with
palindromic segments and a tube structure was constructed
entirely from one species of strand. Such a tubular config-
uration was verified by using AFM (Figure 3 C; Figure S10).
Similar thin tubes were presented in other extended lattices
with different numbers of repetitive motifs (Figures S11 and
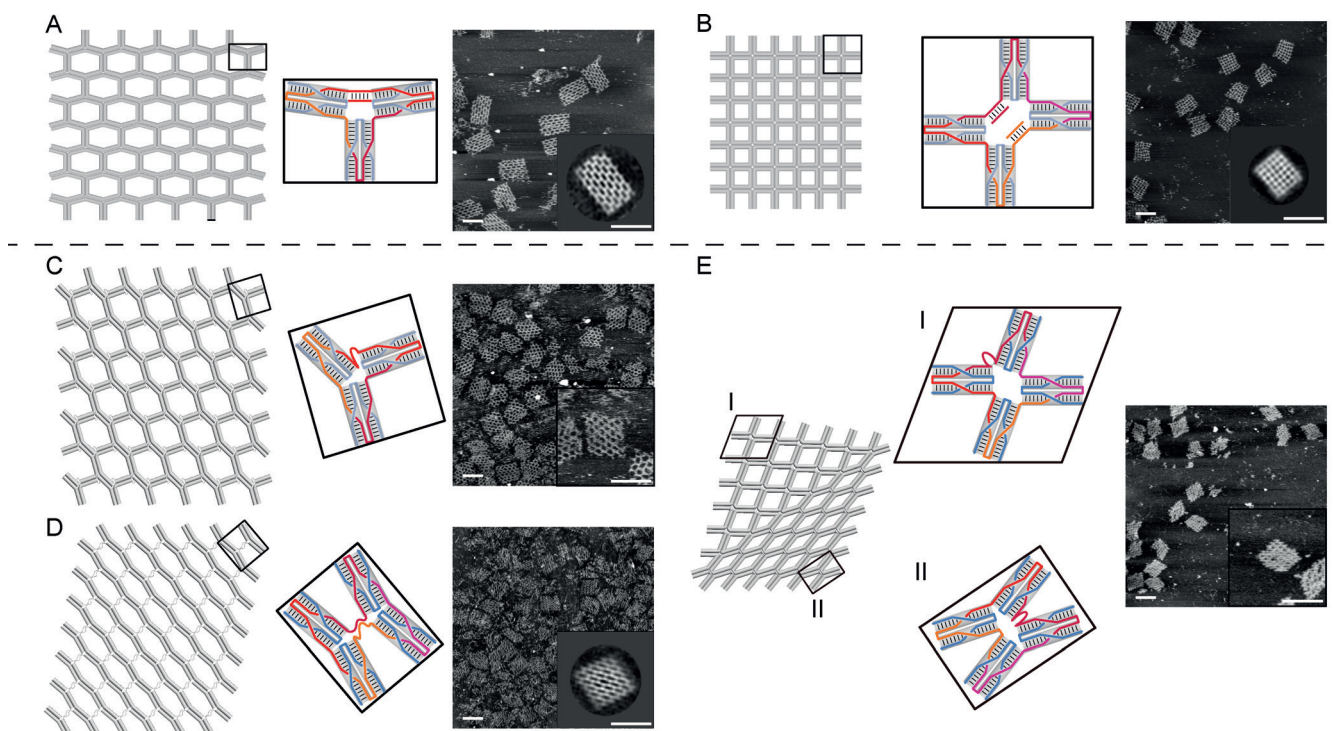S12). The sparse nucleation of small flexible arrays in closed

Figure 2. 2D addressable wireframe structures with angle control. A) From Y-shaped vertices (Figure 1A) to T-shaped vertices (with double-stranded linker at one of the three crossover points of each vertex). B) From X-shaped vertices (Figure 1B) to cross-shaped vertices (with double-stranded linkers at two of the four crossover points of each vertex). C) From Y-shaped vertices (Figure 1A) to irregular 3-arm vertices (with single-stranded linker at one of the three crossover points of each vertex). D) From X-shaped vertices (Figure 1B) to H-shaped vertices (with single-stranded linkers at two of the four crossover points of each vertex). E) From X-shaped vertices (Figure 1B) to chimeric vertices (with single-stranded linker at one of the four crossover points of each vertex). Panels from left to right: Schematics of full wireframe structures, schematics of component motifs, and AFM images (scale bars = 100 nm). Insets: Reference-free class averages calculated from single-particle AFM micrographs [N = 15 in (A), N = 27 in (B) and N = 94 in (D)]. Averaging is not available for structures in (C) and (E) due to the particle heterogeneity.
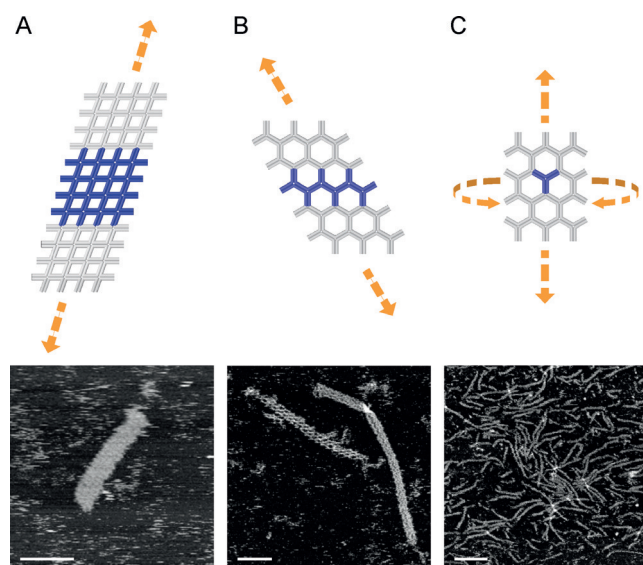

Figure 3. Extended wireframe structures from armed motifs. A) Ribbon from X-motifs extended in 1D. B) Ribbon from Y-motifs extended in 1D. C) Tube structure from one continuous Y-motif extended in 2D. Top: Schematics (repetitive unit cells highlighted in blue). Bottom: The corresponding AFM images (scale bars = 100 nm).

tubular conformation followed by fast growth would lead to the formation of thin tubes. We compared the self-assembly yields of the extended structures composed of different numbers of distinct motifs (i.e., different sizes of repetitive units) by agarose gel electrophoresis. The results revealed a yield decrease in self-assembly with an increasing number of component strands (Figure S13).

Restricted by the polarity of DNA strands (i.e., each strand has a 5' and a 3' end), it is not possible to use the same edge design (odd number of helical half-turns) for triangularly faced polyhedra such as octahedrons and icosahedrons[7] (Figures S14 and S15). Thus, we designed an octahedron and an icosahedron with two bundled DNA duplexes as edges, whose length was modified as an even number of helical half-turns to satisfy the polarity requirement. A DNA octahedron is composed of eight triangles and twelve thin rectangles (phosphodiester bonds as short edges of thin rectangles for illustrative purposes). Two long sides of a thin rectangle are complementary to specific edges from two matching triangles to form a double-duplex edge of the DNA octahedron. As shown in Figure 4A, each triangle is composed of three DNA strands resulting from three nicks, and each thin rectangle is composed of two DNA strands resulting from two nicks. Because of the symmetric arrangements, each DNA strand has three domains (11 nt, 10 nt, and 11 nt, Figure S16). The
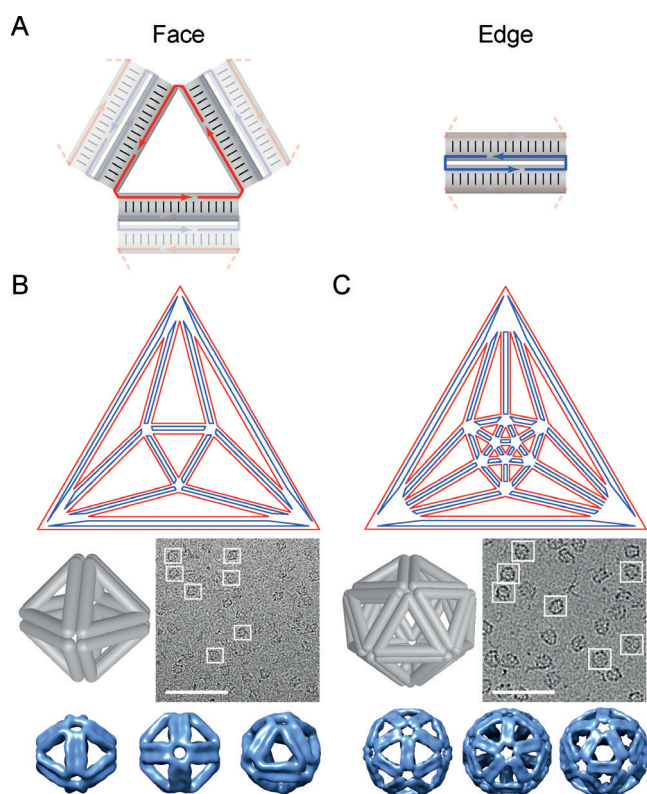
Figure 4. DNA polyhedra. A) Schematics of the representative face and edge in a polyhedron. B) DNA octahedron. C) DNA icosahedron. In (B) and (C), Schlegel diagrams of polyhedra (top panels); cylinder models of polyhedra (center left) and cryo-EM images (center right) (scale bars = 100 nm); different views of 3D maps of DNA polyhedra reconstructed from cryo-EM images on the bottom panels (bottom).

single-stranded linker (i.e., T2) at each vertex of the triangle contour is designed to increase flexibility and the component strands have uniform lengths of 32/34 nt.[1g,2d,h] An octahedron of elongated edge length was also designed and constructed (Figure S17). As a control, component strands without T2 linkers (Figure S18) failed to self-assemble into a desired octahedron. The necessity of including linkers indicates that the flexibility of arms around a certain vertex associated from the linkers enables the arms to fit into a specific geometry. Similar design principles were also applied to construct a DNA icosahedron composed of twenty triangular contours and thirty thin rectangular contours.

The DNA polyhedron samples after gel-based purification were subjected to cryogenic transmission electronic microscopy (cryo-EM) for imaging. The desired octahedron and icosahedron morphologies were observed after 3D reconstruction (Figure 4B,C, bottom panels). The 3D maps also revealed that each edge was composed of two bundled duplexes. Additionally, the resolutions of the well-defined DNA polyhedra in this study are 1.9–2.5 nm (Figures S19–S21), which are comparable to ones constructed from repetitive motifs (at 1–4 nm resolutions).[2h,7,8] In general, the limited resolution the 3D reconstruction of DNA polyhedra is presumably due to the structural flexibility and the corresponding sample inhomogeneity.

Earlier examples in the field have shown that 2D lattices and 3D objects can be constructed by repetitive junction units.[2g,h,9] In order to precisely control the angles between arms, it is necessary to carefully design linker lengths around a certain vertex, and adjust the concentration of the component motifs especially in the formation of a certain type of polyhedron.[2h,7,9b,c,10] With precise molecular design, the minimalist strategy gives rise to extended 2D lattices of different patterns and a collection of polyhedra. On the other hand, most structures presented in this study are constructed with addressable components. In such a maximalist strategy, many more species of strands are involved and structural formation is deterministic without the necessity to fine tune strand concentrations and angles between junction arms.

Yields of nanostructures from the maximalist strategy are in general low and a yield gap is apparent when counterparts from minimalist strategy are available (Table S2). As indicated by the yield decrease for structures with increasing numbers of components (Figure S13 and Table S2), elevated complexity level could contribute to the difficulty of the desired self-assembly. On the other hand, the relative high yields in minimalist self-assembly can be attributed to a careful molecular design and construction (e.g., fine tuning of geometries of junction points and annealing protocols). Similar optimization could be applied to the maximalist self-assembly to achieve higher yields and better structural integrity. These two strategies can be viewed as two complementary design philosophies. The minimalist strategy requires fewer component strands but the molecular design to achieve precisely controlled geometries could be prohibitively challenging; the maximalist strategy enables greater structural complexity with simple molecular design but requires synthesis of a large number of distinct DNA strands. The integration of the two strategies could lead to a cost-efficient construction of nanostructures of high complexity.

As the analogy of LEGO bricks in the macroscopic world goes, when bricks of different shapes and properties are included, one can build sophisticated models more easily. We believe the similar scenario applies to building blocks of structural DNA nanotechnology and that is the rationale behind our development to adopt different motifs, including ones in this study, to build complex DNA nanostructures.[4a,b,d] When building blocks of different fine structural features are available, one can build versatile DNA nanostructures with high levels of controllability, precision, and functionality.

Acknowledgements

Conflict of interest

The authors declare no conflict of interest.

[1] a) P. W. Rothemund, *Nature* **2006**, *440*, 297–302; b) H. Dietz, S. M. Douglas, W. M. Shih, *Science* **2009**, *325*, 725–730; c) S. M. Douglas, H. Dietz, T. Liedl, B. Hogberg, F. Graf, W. M. Shih, *Nature* **2009**, *459*, 414–418; d) Y. Ke, S. M. Douglas, M. Liu, J. Sharma, A. Cheng, A. Leung, Y. Liu, W. M. Shih, H. Yan, *J. Am. Chem. Soc.* **2009**, *131*, 15903–15908; e) D. Han, S. Pal, J. Nangreave, Z. Deng, Y. Liu, H. Yan, *Science* **2011**, *332*, 342–346; f) E. Benson, A. Mohammed, J. Gardell, S. Masich, E. Czeizler, P. Orponen, B. Hogberg, *Nature* **2015**, *523*, 441–444; g) F. Zhang, S. Jiang, S. Wu, Y. Li, C. Mao, Y. Liu, H. Yan, *Nat. Nanotechnol.* **2015**, *10*, 779–784; h) R. Veneziano, S. Ratanalert, K. Zhang, F. Zhang, H. Yan, W. Chiu, M. Bathe, *Science* **2016**, *352*, 1534.

[2] a) N. C. Seeman, N. R. Kallenbach, *Biophys. J.* **1983**, *44*, 201–209; b) J. H. Chen, N. C. Seeman, *Nature* **1991**, *350*, 631–633; c) Y. W. Zhang, N. C. Seeman, *J. Am. Chem. Soc.* **1994**, *116*, 1661–1669; d) H. Yan, S. H. Park, G. Finkelstein, J. H. Reif, T. H. LaBean, *Science* **2003**, *301*, 1882–1884; e) R. P. Goodman, I. A. Schaap, C. F. Tardin, C. M. Erben, R. M. Berry, C. F. Schmidt, A. J. Turberfield, *Science* **2005**, *310*, 1661–1665; f) J. Malo, J. C. Mitchell, C. Venien-Bryan, J. R. Harris, H. Wille, D. J. Sherratt, A. J. Turberfield, *Angew. Chem. Int. Ed.* **2005**, *44*, 3057–3061; *Angew. Chem.* **2005**, *117*, 3117–3121; g) Y. He, Y. Tian, A. E. Ribbe, C. D. Mao, *J. Am. Chem. Soc.* **2006**, *128*, 15978–15979; h) Y. He, T. Ye, M. Su, C. Zhang, A. E. Ribbe, W. Jiang, C. D. Mao, *Nature* **2008**, *452*, 198–201; i) J. Zheng, J. J. Birktoft, Y. Chen, T. Wang, R. Sha, P. E. Constantinou, S. L. Ginell, C. Mao, N. C. Seeman, *Nature* **2009**, *461*, 74–77.

[3] a) Y. Ke, L. L. Ong, W. M. Shih, P. Yin, *Science* **2012**, *338*, 1177–1183; b) B. Wei, M. Dai, P. Yin, *Nature* **2012**, *485*, 623–626; c) L. L. Ong, N. Hanikel, O. K. Yaghi, C. Grun, M. T. Strauss, P. Bron, J. Lai-Kee-Him, F. Schueder, B. Wang, P. Wang, J. Y. Kishi, C. Myhrvold, A. Zhu, R. Jungmann, G. Bellot, Y. Ke, P. Yin, *Nature* **2017**, *552*, 72–77.

[4] a) W. Wang, T. Lin, S. Zhang, T. Bai, Y. Mi, B. Wei, *Nucleic Acids Res.* **2016**, *44*, 7989–7996; b) D. Yang, Z. Tan, Y. Mi, B. Wei, *Nucleic Acids Res.* **2017**, *45*, 3606–3611; c) M. Matthies, N. P. Agarwal, E. Poppleton, F. M. Joshi, P. Sulc, T. L. Schmidt, *ACS Nano* **2019**, *13*, 1839–1848; d) W. Wang, S. Chen, B. An, K. Huang, T. Bai, M. Xu, G. Bellot, Y. Ke, Y. Xiang, B. Wei, *Nat. Commun.* **2019**, *10*, 1067.

[5] H. P. Liu, Y. Chen, Y. He, A. E. Ribbe, C. D. Mao, *Angew. Chem. Int. Ed.* **2006**, *45*, 1942–1945; *Angew. Chem.* **2006**, *118*, 1976–1979.

[6] a) Y. Cui, R. Chen, M. Kai, Y. Wang, Y. Mi, B. Wei, *ACS Nano* **2017**, *11*, 8199–8206; b) J. Song, Z. Li, P. Wang, T. Meyer, C. Mao, Y. Ke, *Science* **2017**, *357*, eaan3377.

[7] P. Wang, S. Wu, C. Tian, G. Yu, W. Jiang, G. Wang, C. Mao, *J. Am. Chem. Soc.* **2016**, *138*, 13579–13585.

[8] a) C. Zhang, M. Su, Y. He, X. Zhao, P. Fang, A. E. Ribbe, W. Jiang, C. Mao, *Proc. Natl. Acad. Sci. USA* **2008**, *105*, 10665–10669; b) Y. He, M. Su, P. A. Fang, C. Zhang, A. E. Ribbe, W. Jiang, C. Mao, *Angew. Chem. Int. Ed.* **2010**, *49*, 748–751; *Angew. Chem.* **2010**, *122*, 760–763.

[9] a) D. Liu, M. Wang, Z. Deng, R. Walulu, C. Mao, *J. Am. Chem. Soc.* **2004**, *126*, 2324–2325; b) Y. He, Y. Chen, H. P. Liu, A. E. Ribbe, C. D. Mao, *J. Am. Chem. Soc.* **2005**, *127*, 12202–12203; c) Y. He, Y. Tian, Y. Chen, Z. X. Deng, A. E. Ribbe, C. D. Mao, *Angew. Chem. Int. Ed.* **2005**, *44*, 6694–6696; *Angew. Chem.* **2005**, *117*, 6852–6854.

[10] L. Liu, Z. Li, Y. Li, C. Mao, *J. Am. Chem. Soc.* **2019**, *141*, 4248–4251.